Journal of Chemical Health Risks

www.jchr.org

JCHR (2024) 14(1), 330-346 | ISSN:2251-6727

In-Vitro and In-Vivo Characterization of Hyaluronic Acid Composite Gel with Anti-Inflammatory Activity for Infected Wound Healing

Pratibha Sahu[1], Rinkee Verma[2], Kiran Singh[2], Chandrika Ahirwal[3], Geetanjali Sahu[4], Akhilesh Kumar Sahu[5], Jhakeshwar Prasad[6]*

[1, 6]*Shri Shankaracharya College of Pharmaceutical Sciences, Junwani – 490020, Bhilai, Chhattisgarh, India

[2]Rungta College of Pharmaceutical Sciences and Research, Raipur – 492099, Chhattisgarh, India

[3]Faculty of Pharmacy, Chandkhuri - 491001, Durg, Chhattisgarh, India

[4]Shri Shankaracharya Professional University, Junwani - 490020, Bhilai, Chhattisgarh, India

[5]Chhatrapati Shivaji Institute of Pharmacy, Durg – 491001, Chhattisgarh, India

*Corresponding author: - Jhakeshwar Prasad

*Shri Shankaracharya College of Pharmaceutical Sciences, Junwani – 490020, Bhilai, Chhattisgarh, India,

(Received: 27 October 2023 Revised: 22 November Accepted: 26 December)

Keywords:
Antimicrobial peptide;
Hydrogel;
Wound healing;
Anti-inflammatory

Abstract:

Bacterial biofilm formation and drug resistance are common issues associated with wound healing. Antimicrobial peptides (AMPs) are a new class of antimicrobial agents with the potential to solve these global health issues. New injectable adhesive antibacterial hydrogels have excellent prospects of becoming the next innovative wound-healing dressings. In this study, the hyaluronic acid was connected to the antibacterial peptide Plantaricin 149 (Pln149), obtaining HAD, AMP. HAD, AMP performed well in efficient antimicrobial activity, good histocompatibility, low drug resistance, low bacterial biofilm formation, and fast wound healing process which are essential for rapid healing of infected wound. During the hydrogel degradation process, Pln149 was released to inhibit bacterial communication and reduce bacterial biofilm formation. Meanwhile, HAD, AMP could upregulate anti-inflammatory and pro-angiogenic factors, and down-regulate inflammatory factors to promote the healing of infected wounds, which provide a new idea for skin healing strategies.

1. Introduction

Skin is the first immune barrier of the body to prevent microorganism invasion [1]. The subcutaneous tissue is deprived of protection after skin damage, and then the exposed wound will be contaminated within 8 h. If the wound is seriously infected, bacterial biofilm can easily form when the bacterial concentration reaches 106 colony-forming units (CFU) [2]. Skin and soft tissue lesions are likely to aggravate during disease development, and serious patients even acquire an infection. [3]. *Staphylococcus aureus* (*S. aureus*) is the leading source of skin and soft tissue infection [4], while Meticillin-resistant *Staphylococcus aureus* (MRSA) accounts for a large proportion of clinical *S. aureus* infections. MRSA has strong pathogenicity and a wide range of transmission routes, which can lead to a variety of tissue and organ infections, sepsis, shock, and other serious complications [5]. Once MRSA biofilms formed, the infection treatment becomes considerably challenging. At present, vancomycin is the most common drug in MRSA clinical treatment, and known as “the last line of defense against drug-resistant strains” [6]. However, vancomycin is highly unstable at room temperature and does have some side effects [7]. Antimicrobial peptides (AMPs) are a potential new class of antimicrobial agents, and have become a potential solution to the global antibiotic resistance problem [8]. Although the AMPs antimicrobial mechanism is not completely clear, it is generally believed that they act on the bacterial cell membrane forming ion channels. These ion channels eventually destroy the membrane integrity, leading to cell content leakage, and consequent cell death. AMPs not only show strong bactericidal effect, but also present broad spectrum antibacterial activity [9]. In

Journal of Chemical Health Risks

www.jchr.org

JCHR (2024) 14(1), 330-346 | ISSN:2251-6727

addition, they can improve immunity and accelerate wound healing [10].

In the human body, skin tissue is the largest, most exposed, and most vulnerable tissue. Once skin tissue is damaged, the repair process is very complex, including four important overlapping stages: hemostasis, inflammation, proliferation, and remodeling/maturation [11]. Although most skin lesions can heal quickly and effectively within 1 or 2 weeks, extensive full-thickness wounds often have difficulty in healing, seriously impacting patients' health and even threatening patients'lives. Therefore, various biomaterials have been developed as wound dressings, such as nanofibers, sponges, foam, and hydrogels [12]. Therefore, a variety of newly developed biomaterials have been used as wound dressings, among these materials, injectable polymer hydrogels have become a promising choice because of their adjustable physical and chemical properties, their similarity to extracellular matrix (ECM), and their ability to fill any irregularly shaped wound [13]. In particular, injectable antibacterial hydrogels can adhere and bond to defective tissues, thereby accelerating wound healing [14]. They can also contribute to hemostasis as a sealant to stop bleeding or prevent liquid or gas leakage from the wound and play a protective role to avoid bacterial infection [15]. Hydrogel is a macromolecular polymer gel synthesized by physical, ionic, or covalent crosslinking of polymer chains. It can absorb a large amount of water through hydrogen bonding. For this reason, they can be used as drug delivery systems with designed preferred characteristics. Ideal hydrogels can selectively release drugs according to physical changes such as temperature and pH [16]. Composite hydrogels are huge three-dimensional network polymers combined with each other through chemical or physical crosslinking. Their hydration and porous structure can simulate the tissues inherent characteristics, structure, and microenvironment. Composite hydrogels with improved properties can be obtained through functional groups in the polymer structure [17]. Therefore, developing a new injectable, adhesive and antibacterial hydrogel dressing can provide excellent prospects for the wound healing process. In this study, we describe an injectable and light curable hyaluronic acid composite gel with the antimicrobial peptide Plantaricin 149 (Pln149). Pln149 is a bacteriocin produced by *Lactobacillus plantarum* NRIC 149 isolated from pineapple and our previous research have reported that Pln149 has a inhibitory effect on bacterial biofilm formation [18]. Our study to achieve antibacterial function and promote healing in vivo. We also present a novel preparation method for an antibacterial drug-loaded hyaluronic acid composite gel for accelerating infected wound healing.

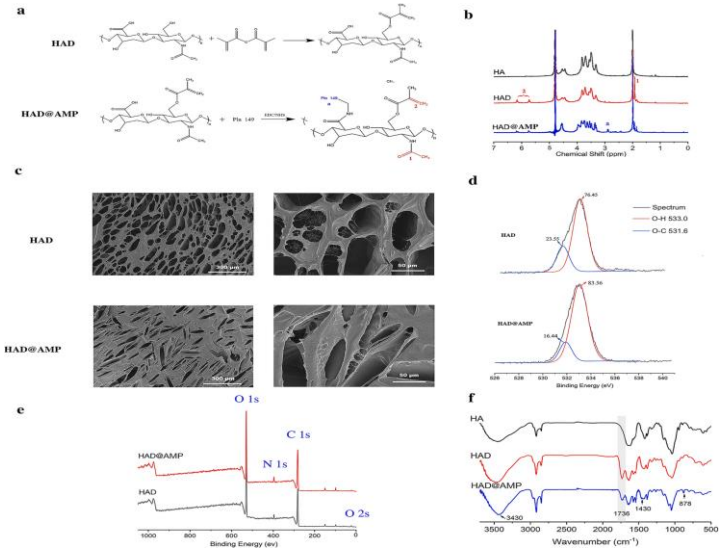

Fig.1. HAD and HAD, AMP characterization. (a) the reaction of HAD and HAD, AMP, (b) Nuclear magnetic resonance (NMR) of HAD and HAD, AMP hydrogel, (c) Field emission scanning electron microscopy (FESEM) images of HAD and HAD, AMP hydrogel, (d, e) X-ray photoelectron spectroscopy (XPS) of HAD and HAD, AMP hydrogel, (f) Fourier transform infrared spectrophotometry (FTIR) of HAD and HAD, AMP hydrogel.

Journal of Chemical Health Risks

www.jchr.org

JCHR (2024) 14(1), 330-346 | ISSN:2251-6727

2. Material and methods

2.1. Materials and reagents

Hyaluronic acid (HA, Mw = 20 ~ 40WDa), methacrylic anhydride (MA), *N*, *N*-dimethylformamide (DMF), ethanol, 1-ethyl-(3-dimethylaminopropyl) carbon diimide hydrochloride (EDC), N-hydroxysuccinimide (NHS), hydrochloric acid, and 2-hydroxy-4′-(2-hydroxyethoxy)-2-methylphenylacetone were purchased from New Delhi, India. Pln149 was synthesized by Nanjing Apeptide Co. Ltd. (New Delhi, India). The peptide was purified by high-performance liquid chromatography, and its identity was verified by SDS-PAGE. The purity of Pln149 (>95 %) and mass were confirmed by electrospray ionization mass spectrometry.

2.2. HAD hydrogel synthesis

An unsaturated double bond was grafted into HA to obtain an HAD hydrogel by esterification reaction with methacrylic anhydride and hydroxyl group in the HA side chain. The specific reaction principle is shown in Fig. 1. 500 mg sodium hyaluronate was completely dissolved by stirring in ultrapure water at 2 % *W*/*V* for 4 h at room temperature. Dimethylformamide (DMF) was then added in drops to the solution (volume ratio water: DMF = 3:2) and stirred well, and the mixture was cooled to 4 ◦C. Methacrylic anhydride was added to the mixture in 3:1 amounts (MA:HA = 3:1), and the reaction was maintained for 24 h at a pH between 8 and 9 through 0.5 mol/L NaOH solution. The polymer was precipitated by adding ethanol, dissolved in ultra-pure water, and dialyzed in pure water (dialysis bag molecular weight cut off = 14 KDa) for 3 days. Purified HAD was recovered by freeze-drying for later use.

2.3. HAD, AMP hydrogel synthesis

Lyophilized HAD was dissolved in deionized water at a concentration of 1 % *W*/*V* for 2 h, and the pH value was adjusted to 5.5 with 0.5 mol/L HCl. The reaction was protected by using a continuous nitrogen flow to prevent oxygen from interacting with the solution. Then, EDC and NHS were added to the solution by mass ratio HAD: EDC: NHS = 1:3: 3. After stirring for 30 min, AMPs in the same proportion as HAD were added to the mixed solution in an oxygen-free environment, and the pH value was maintained at 5.5 for 4 h. The reaction was allowed to stir at room temperature overnight. Unreacted chemicals and by-products were removed by dialyzing in an acidic aqueous solution (HCl solution at pH 5.5) for 3 days. The HAD, AMP solution was freeze-dried and stored at - 20 ◦C for later use. The freeze-dried samples were dissolved in deionized water at a concentration of 3 % *W*/*V*, and a photoinitiator I2959 at 0.5 % W/V was added and mixed uniformly. The hydrogel was formed by cross-linking below the UV light source (wavelength 365 nm, intensity 18 mW/cm2) for 10 min [19]. Membranes' chemical composition was characterized by Fourier transform infrared spectrophotometry (FTIR, Bruker vector 22, Germany); blended with a potassium bromide pellet, 64 scans were recorded for each spectrum at a resolution of 4.0 cm- 1, and proton nuclear magnetic resonance (1H NMR) spectroscopy (Bruker AVANCE III 500, Mumbai, India; 40 ◦C in deuterated H2O).

2.4. Field emission scanning electron microscopy (FESEM)

The hydrogel surface morphology was observed via field emission scanning electron microscopy (Nova Nano 450, Thermo FEI, Mumbai, India) at an accelerating voltage of 5 kV with platinum sputtering.

2.5. X-ray photoelectron spectroscopy (XPS)

Changes in the chemical bonds on the hydrogel surface were characterized by X-ray photoelectron spectroscopy (AXIS Supra, Mumbai, India). All spectra processing was carried out with the ESCApe software. The C 1 s photoelectron peak at 284.8 eV was used as a binding energy correction.

2.6. Rheology of HAD, AMP

The rheological properties of HAD, AMP were measured by using a Haake Mars 60 rheometer (Thermofisher, Waltham, Mumbai, India) with cone plate system (diameter, 35 mm; angle, 2◦). The range of frequency was from 0.01 to 10 Hz. The experimental temperature was 37 ◦C.

2.7. Differential scanning calorimetry (DSC)

The thermal properties of hydrogel lyophilized samples were measured by DSC under nitrogen atmosphere (nitrogen flow rate was 50 mg/ml). Approximately 10 mg of samples were heated at a rate of 10 ◦C/ min, and individual hydrogel weight variations were recorded.

2.8. Swelling performance test

The swelling properties of freeze-dried hydrogel scaffolds were tested. An analytical balance was used to weigh and record the original weight of each hydrogel (Wa), then the hydrogels were placed in PBS

Journal of Chemical Health Risks

www.jchr.org

JCHR (2024) 14(1), 330-346 | ISSN:2251-6727

at 37 ◦C to observe the swelling changes of the hydrogels. Samples were taken at 2 h, 4 h, 12 h, 24 h, 48 h and 72 h, and the water on the surface of the hydrogels was absorbed by filter paper. The weight of hydrogel samples (Wb) was weighed and recorded, and three duplicate samples were set for each group. The swelling degree (W) of hydrogel can be calculated by the following formula:

The degree of swelling (W) = *Wb - Wa Wa* *100%

The swelling ratio is a crucial parameter to evaluate the swelling capacity of hydrogels.

2.9. Amp release tests

The release behaviours of AMP HAD, AMP samples were determined by placing them in 2ml PBS (Vo) at 37 ◦C with continuous shaking. At predetermined time intervals (*n* = 1, 2, 3, 7, 10days), 1ml of the initial buffer was removed for analysis followed by the addition of 1ml fresh PBS. The amount of AMPs in the release medium was detected using the Microplate Reader at a wavelength of 270nm. Cumulative AMP release profiles were calculated, and the total amount of AMPs encapsulated in HAD was calculated by the equal quality antimicrobial peptides in HAD, AMP dissolved in PBS. The cumulative release rate was calculated with the following formula:

The cumulative amount of release (%) = Ct C∞ × 100%

Where, t is the Pln149 amount released at time t, while C∞ is the total.

Pln149 amount.

Cell Culture.

The isolation of rat Bone Marrow Stromal Cells was carried out based on previously study [20] BMSCs were cultured in low-glucose DMEM (Sigma-Aldrich) containing 10 % FBS. Mouse fibroblast cells (L929) were sourced from the Procell Technology Co., Ltd. (Mumbai, India) and cultivated in 10 % FBS-supplemented high glucose DMEM (Sigma-Aldrich). All cells were cultured at a 37 ◦C and 5 % CO2 incubator with a humidified atmosphere.

2.10. Cell viability evaluation

L929 mouse fibroblasts and rBMSCs were selected as test cells and were seeded in 96-well plates at a 5 × 10 3 cells/well density respectively. Cultivating in respective medium with leachate of HAD and HAD, AMP hydrogel at concentration of 100 μg/ml, the group that did not add any leachate served as control and using PBS as the blank. The Cell Counting Kit-8 (CCK-8, Dojindo Laboratories, New Delhi, India) assay was used to evaluate cell cytotoxicity and cell proliferation at different time point of 1, 3 and 5 d in triplicate. After CCK-8 solution was added to each well and further incubated for 2 h at 37 ◦C. The absorbance of each well was recorded by a microplate reader (Multiskan MK3, Thermo, USA) at 450 nm. The cell compatibility was measured by Live/Dead cell staining kit (Solarbio, Beijing, China), The L929 and rBMSCs with a density of 2×104 cells/well were seeded in 24-well plates respectively, and the culture conditions and experimental grouping were similar to CCK-8 assay. Calcein acetoxymethyl ester (CA-AM) and propidium iodide (PI) were used to stain live cells in green and the dead in red at different time point of1, 3 and 5 d in triplicate according to the manufacturer's instructions, then observe samples under fluorescence microscope (Zeiss LSM 710, New Delhi, India).

2.11. Hemolytic test

Collect fresh blood from a healthy Sprague-Dawley (SD)-rat and reserved into the anticoagulant tube. Fresh blood (1 ml) was washed three times with 20 ml PBS by centrifugation (2500 rpm, 10 min) and discarded upper serum. The centrifuged red blood cells were resuspended with 20 ml PBS then centrifuge another three times. Diluted 750 μl red blood cell suspension were added to 250 μl different. Samples (HAD, HAD, AMP, TritonX-100, PBS)and incubated at 37 ◦C for 4 h and then centrifuged at 10000 rpm for 10 min. The supernatant was collected and transferred to a 96-well plate and absorbance was measured at 545 nm using a microplate reader (Multiskan MK3, Mumbai, India). Calculate the average of the three measurements. TritonX-100 was used as positive control and PBS as the negative control. The hemolysis rate is calculated according to the following formula:

Hemolysis ratio (%) = ODtest-ODneg OD pos-ODneg × 100%

2.12. Strains and culture conditions

Methicillin-resistant *Staphylococcus aureus* (MRSA, ATCC 33591) was purchased from ATCC. MRSA was grown overnight in Brain Heart Infusion media in a microaerophilic environment (5 % CO2) at 37 ◦C. Then, the MRSA suspensions were centrifuged at 2000 rpm for 5 min, and the final concentrations of the cultures were adjusted to 1 × 106 CFU/ml.

2.13. HAD, AMP antibacterial activity test

Journal of Chemical Health Risks

www.jchr.org

JCHR (2024) 14(1), 330-346 | ISSN:2251-6727

The antibacterial efficacy of HAD, AMP was evaluated by the disk diffusion method [21] and colony count on plates. MRSA was first grown on columbia sheep blood agar under microaerophilic conditions at 37 ◦C for 24 h and then transferred into BHI at a concentration of 0.5 McFarland (MCF) (1.5 × 108 CFU/ml). For the disk diffusion assay, the vitro-release solutions from HAD, AMP on the first day were used to make the paper disk, and HAD, AMP, vancomycin, clarithromycin and ceftriaxone filter paper disks (6 mm diameter) were spaced upon the nutrient agar plates cultured with MRSA. After 18h incubation, the zones of growth inhibition surrounding the paper disks were measured to evaluate the antibacterial efficacy of HAD, AMP. In addition, the 1 ml HAD, AMP and 500 µl MRSA suspensions were added in sterile tubes containing 5 ml BHI, and the colony count were conducted after 12 and 24 h culture under microaerophilic conditions at 37 ◦C.

2.14. HAD, AMP anti-biofilm effects

For this assay, 300 µl of MRSA suspensions were transferred to a sterile 48-well plate with 200 µl BHI broth or either 200 µl HAD, AMP/well. The plates were incubated under microaerophilic conditions at 37 ◦C. Biofilm formation was examined after 24 h incubation and prepared for examination according to the previous methods [22]. Biofilm specimens after 24 h were stained with Live/Dead BacLight Bacterial Viability Kit (Invitrogen, Mumbai, India). Biofilms were observed under a laser confocal microscope (Zeiss LSM 710, Mumbai, India). All the biofilm images were captured and saved using Zen 2010 Light Edition (Carl Zeiss, Mumbai, India). The biofilm integrated optical density (IOD) was evaluated by using ImageJ software.

2.15. Transcriptome Analysis of HAD, AMP-treated MRSA

In order to gain additional insight into the different communication regulators in MRSA isolates, we next examined the gene expression profiles of the original MRSA strain and compared them with HAD, AMP-treated MRSA. MRSA incubated for 8 h with 62.5 µg/ml HBPL or with only BHI (control) were used for transcriptome sequencing. The Library preparation and sequencing were completed by the Majorbio Company. Kyoto Encyclopedia of Genes and Genome (KEGG) analysis was performed using KEGG Mapper. Heat maps of the differentially expressed genes were constructed using Graphpad Prism 8.

2.16. Transcriptome Analysis of HAD, AMP-treated L-929 mouse fibroblasts

In order to gain additional insight into the different antiinflammatory, pro-inflammatory, and growth regulators profile after HAD, AMP treatment, we next moved to examine the gene expression profiles in L-929 mouse fibroblast. The L-929 mouse fibroblasts incubated with high-glucose DMEM with 100 µg/ml HAD, AMP and 100 ng/ml lipopolysaccharide (LPS; Sigma) for 3 days were used for transcriptome sequencing and a control with no treatment. Total RNA was purified from each cell culture using TRIzol according to the manufacturer's instructions. RNA was reverse-transcribed with SuperScript III Reverse Transcriptase and digested with RNaseH. Second-strand synthesis was carried out using DNA polymerase according to the manufacturer's instructions.

2.17. Western blotting

Cells in different groups(control, plate, HAD and HAD, AMP) were washed with PBS three times, lysis buffer (Thermo Fisher Scientific, Mumbai, India) and 1 % Protease Inhibitor (Sigma) was used to harvest total proteins. Then quantify the concentration of proteins by BCA kit (Thermo Fisher Scientific, Mumbai, India). After electrophoretic separation by SDS - PAGE, proteins were transferred onto polyvinylidene fluoride membranes (Bio-Rad, USA) that were blocked using 5 % non-fat milk for 1 h at room temperature. Membranes were incubated with primary antibodies against TNF-α, IL-6 (21865-1- AP, Proteintech, USA), TGF-β1, β-actin overnight at 4 ◦C. After incubation, membranes were washed three times in TBST (Tris-buffered saline and Tween 20) and incubated with respective appropriate secondary antibodies for 1 h, the membranes were washed twice in TBS with 0.1 % Tween-20. After washing, protein bands were visualized using an ECL kit. ImageJ software was used for further analysis.

2.18. Reverse transcription-quantitative PCR analysis

Based on the Transcriptome Analysis of HAD, AMP-treated L-929 mouse fibroblasts, three candidate mRNAs (TNF-α, IL-6, and TGF-β1) were selected for further reverse transcription-quantitative PCR analysis.

Journal of Chemical Health Risks

www.jchr.org

JCHR (2024) 14(1), 330-346 | ISSN:2251-6727

Separation of total RNA from different grouping cells by using the Trizol reagent (Thermo Fisher Scientific) as instructed by the manufacturer. Reverse transcription procedure was performed with 1 µg of total RNA in a final volume of 20 µl using the Hifair II Strand cDNA Synthesis Kit. Primers for TNF-α, IL-6, and TGF-β1 were designed using Primer-BLAST software from the National Center for Biotechnology and synthesized by Shenggong. β-Actin was used as a housekeeping gene for normalization. The primers used for gene amplifications are displayed in Table 1 (Supplementary data). The expression level of target genes was quantified using a SYBR Green Master Mix kit on Applied Biosystems (ABI) 7500 Fast real-time PCR system (Thermo Fisher Scientific).

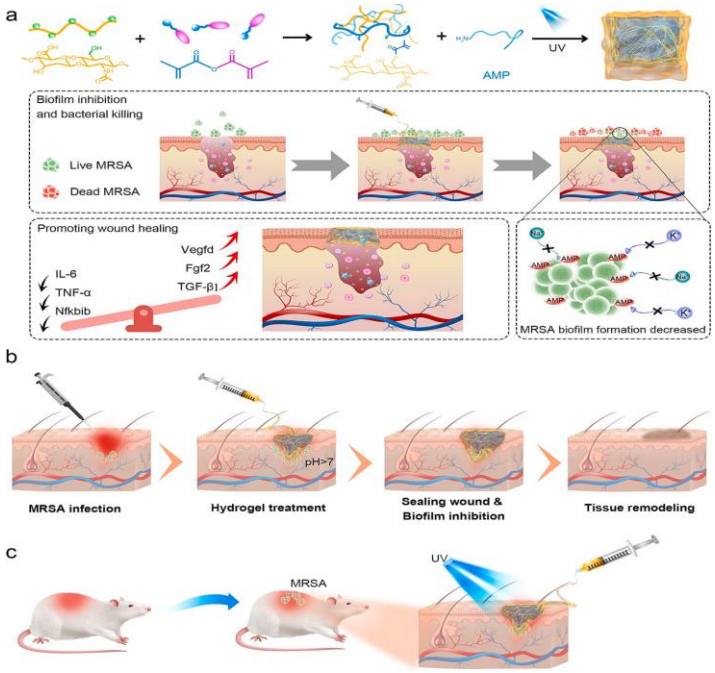

Fig.2. Hyaluronic acid composite gel preparation and accelerating the wound healing process. a) Pln149 encapsulated in hyaluronic acid composite gel (HAD, AMP) antimicrobial biofilm and wound healing promotion mechanisms. b) Wound healing process after hydrogel treatment and c) in vivo tests.

2.19. In vivo models

Twenty-four SD rats (female, 200-250 g in weight) were purchased from Shanghai Slack Experimental Animal Company (Shanghai, China). The rats were kept in a regulated environment and supplied with abundant water and food. SD rats were anesthetized via intraperitoneal injection of Pentobarbital (30 mg/kg). The dorsal hair of each rat was shaved before surgery. A 10 mm diameter full-thickness round wound was created on the back of the rat by a skin biopsy punch. Subsequently, 40 µl of MRSA suspension (1 × 106 CFU/ml) was added to the wound site. The rats were randomized into three groups (eight rats/group): control, HAD treatment, and HAD, AMP treatment. All of the wounds of rats were then covered with a Tegaderm Films (3 M, USA) to prevent the hydrogel from shedding or rat scratches. The wounds in all groups were photographed on days 0, 3, 5, 7 and the 10th day. The wound area was measured and analyzed using Image J analysis software. The ratio of wound closure (%) was defined as the ratio of the healed wound area to the initial wound area, and the healed area = initial wound area - present wound area. The experimental process was shown in fig.2.

2.20. Histological analysis and Immunohistochemical staining study

To assess the wound healing process, histological studies of the wound sites were performed on day 10. Skin tissue from the wound sites was obtained, fixed, embedded in paraffin, and sectioned, following the appropriate protocols. The sections were stained with hematoxylin and eosin (H&E) and Masson's trichrome

Journal of Chemical Health Risks

www.jchr.org

JCHR (2024) 14(1), 330-346 | ISSN:2251-6727

to evaluate wound closure and collagen formation. Immunohistochemical staining of tumor necrosis factor-α (TNF-α), transforming growth factor-beta1 (TGF-β1) and PECAM-1(CD31) were performed to assess the inflammatory reaction and number of new blood vessels in tissues after 10 days of surgery. The epidermis thickness were measured by a calibrated ruler. The dermal collagen deposition was measured and expressed as collagen volume fraction. All histological and immunohistochemical staining images were captured with an Olympus Digital Slice Scanner VS200.

2.21. Statistical analysis

Results values were shown as mean ± standard deviation. Data among different groups were analyzed using one-way analysis of variance (ANOVA) (SPSS 25.0 software, IBM, USA). Statistical significance was set to $P < 0.05$ (*), 0.01 (**), and 0.001 (***).

3. Results and discussion

3.1. HAD, AMP characterization and biocompatibility test

The chemical reaction were shown Fig. 1a. The chemical structure of the synthesized polymers and hydrogels were characterized by NMR and FT-IR. As shown in Fig. 1b, HA, HAD, and HAD, AMP structures were characterized by 1H NMR using D2O as solvent: the peak at 4.79 ppm is the characteristic peak of D2O; the peak at 3–4 ppm of proton hydrogen in HA sugar ring structure; the peak at 2.01 ppm of methyl H on the side chain of the *N*-acetylglucosamine. When comparing HA NMR, HAD showed the peak at 5.73 ppm, and two new peaks appeared at 6.16 ppm, the characteristic peaks of an olefin proton in the methacrylic anhydride. The peak at 1.93 ppm is the expected peak of methyl H adjacent to the amide, indicating that the methyl methacrylate is connected to hyaluronic acid. After adding AMP Pln 149, NMR showed the peak at 2.89 ppm, a characteristic peak representing lysine, indicating the successful reaction between AMP and HA. Under the SEM observation, as shown in Fig. 1c, all the hydrogel samples exhibited a three- dimensional porous structure. Generally, the pore size of HAD, AMP hydrogel did not change significantly compared with that HAD hydrogel without antibacterial peptides. After the introduction of antibacterial peptides in hydrogel, the intermolecular forces (hydrogen bonds and van der Waals forces) of macromolecules became stronger, and the pore structure was pulled into a slender shape under constraint. Injectability of hydrogels used as a wound dressing is vital to accommodate irregularly shaped wounds. The wide spectrum of XPS (Fig. 1d and e) showed the main chain structure were identical. The O 1 s spectrum showed peaks at 533 and 531.6 eV, which were assigned to O–H and O–C, respectively.

HAD group had higher signal (23.55 % in HAD vs. 16.44 % in HAD, AMP) at 533 eV and lower signal (76.45 % in HAD vs. 83.56 % in HAD, AMP) at 531.6 eV than HAD, AMP, revealed that the replacement of the side chain's hydroxyl by Pln 149, confirmed the successful connection of AMP. From the infrared spectrum in Fig. 1f, we were able to understand that HA has a robust stretching vibration peak near 3300 cm- 1, corresponding with the O–H absorption band of the side chain's hydroxyl. There was a stretching vibration absorption peak of -CH2- near 2920 cm- 1; and an absorption band near 1415 cm- 1 indicating the existence of an acetyl amino structure. Both 1038 and 948 cm- 1 showed CO-C stretching vibration bands. The modified HAD and HAD, AMP both contained these stretching vibration absorption peaks of HA, indicating that the main structure had not changed. The ester bond in the modified HAD formed a new vibration absorption peak at 1736 cm- 1, which belongs to the absorption vibration characteristic peak of -C=O- , indicating that methacrylic anhydride was successfully bound to HA. A sharp peak appeared at 3430 cm- 1 and moved to low frequency, representing the stretching vibration of an aliphatic NH2, while a peak appeared at 878 cm- 1 representing the bending vibration. AMP was successfully inserted into HAD, revealed by the peak at 1430 cm- 1 representing the stretching vibration of C– –C on the benzene ring. As illustrated in Fig. 2a, HA hydrogels incorporated with or without Pln 149 were successfully fabricated, termed as HAD hydrogel (HAD), and HAD, AMP hydrogel. The injectable property of HAD, AMP hydrogel was shown in Fig. 2b, the photo images revealed ostensively that the HAD, AMP hydrogel could be sucked into a 1 ml syringe and then injected out at room temperature to form set shapes (letters, numbers, fill a mold) and be cured by light in minutes. The storage modulus (G′) and the loss modulus (G″) for 5.0 wt% HAD, AMP solution at a

Journal of Chemical Health Risks

www.jchr.org

JCHR (2024) 14(1), 330-346 | ISSN:2251-6727

frequency of 0.01–01 Hz was shown in Fig. 2c. Both G′ and G″ of HAD and HAD, AMP showed an increase as the frequency increases.

The values of G′ were always smaller than and the G″ of the two hydrogel indicated that HAD and HAD, AMP hydrogel remained liquid at 37 ◦C. Compared with the HAD group without antimicrobial peptides Pln 149, the G′ and G″ were not significantly different, indicate that after chemical combined with the antimicrobial peptide, the HAD, AMP still showed good flow properties at 37 ◦C. Figs. 2d display the DSC heat flow curve for two hydrogels chosen to display the shapes of the peaks determined in dynamic mode at different heating rates and sample masses. The figures show the peak values of the HAD, AMP groups shifted toward higher temperatures compared to the value of HAD groups. Fig. 2e shows the swelling ratio (SR) of HAD and HAD, AMP gels as a function of time in the neutral solution. For both two gels, the SR increased quickly during the first 12 h and then gradually got into slow trend. The equilibrium swelling of both gels were obtained after 24 h. The primary bond and the amide bond of HAD, AMP can be broken in an acidic environment, Fig. 2f shows antimicrobial peptides were released continuously for 10 days in HAD, AMP hydrogel. HAD, AMP biocompatibility is one of the most important factors to be considered for its direct application on the infected wound area. In order to ensure whether HAD, AMP released at the wound sites caused toxicity, HAD, AMP biosafety was evaluated by in vitro cytotoxicity assay and blood biochemistry study. BMSCs could express hVEGF165/hBD3 to promote wound healing, therefore we also use BMSCs in cytotoxicity assay [23]. After 1, 3, and 5 days of culture, there was no significant difference in L929 and rBMSCs cell viability or proliferation between the HAD, AMP and control groups (Fig. 2g and h). The hemolysis ratio was measured to further validate the hydrogel's blood compatibility. After incubation with the HAD, AMP hydrogel, no apparent hemolysis was observed, and hemolysis ratios were <5 % (Fig. 2i) within the normal hemocompatibility range. These results demonstrate that treatment of wound sites with HAD, AMP would not exert any systematic toxicity. The remarkable biocompatibility of HAD, AMP hydrogel holds great promise to become the next wound dressing.

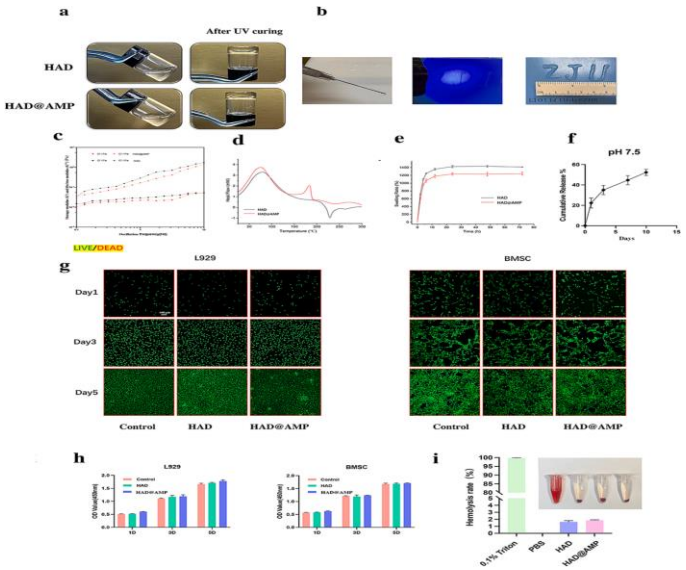

Fig.3. (a) Photograph of HAD and HAD, AMP hydrogel before and after UV curing. (b) Injectability and light curing capacity of HAD, AMP. (c) Variations of G′ and G″ with oscillation frequency for the hydrogels (d) DSC curves of HAD gels and HAD, AMP gels. (e) The swelling ratio of HAD gels and HAD, AMP gels as a function of time. (f) Cumulative release of HAD, AMP after 1, 2, 3, 7, 10 days. (g) Confocal laser microscopy results after Live/Dead staining in vitro biosafety studies, (h) optical density (OD) value of L929 and BMSCs for 1,3 and 5 d. (i) Hemolysis ratio (%) of different groups and hemolysis activity assay.

Journal of Chemical Health Risks

www.jchr.org

JCHR (2024) 14(1), 330-346 | ISSN:2251-6727

3.2. HAD, AMP hydrogel on MRSA: antibacterial and anti-biofilm activity and transcriptome analysis

Evaluating HAD, AMP application in infected wound healing was essential to test its antibacterial and anti-biofilm activity. MRSA is one of the most important pathogens in the clinical infection field. It has strong pathogenicity and a wide range of transmission routes, which can lead to a variety of tissue and organ infections, sepsis, shock, and other serious complications [24]. As the inhibition zone test showed (Fig. 3a and b), HAD, AMP exerted almost the same antibacterial effect on MRSA as vancomycin. Vancomycin has traditionally been the last line of defense against MRSA but still relegated to the spread of current drug-resistant strains [25]. Bacterial biofilms are thought to be responsible for challenging the cure of most infectious diseases [26]. Therefore, removing bacterial biofilm is of great significance for treatment. Inside bacterial biofilms, bacteria can communicate through ion channels. After the ion channel is blocked, communication between bacteria no longer exists. This means that antiarrhythmic drugs can inhibit bacterial biofilm growth since they are mainly sodium and potassium channel blockers [27]. In our previous study, Pln149 can inhibit the potassium channel so we continue to use this antibacterial peptide for this study. In antibacterial biofilm experiments, HAD, AMP inhibited the biofilm formation significantly after 24 h compared with HAD groups and control groups (Fig. 3 c and e, $P < 0.05$). For the Live/dead ratio (Fig. 3d), there are no obvious differences in three groups, in fact, the antimicrobial peptides reduce the adhesion of bacterial biofilms, therefore, the dead bacteria were also few in the HAD, AMP group. *S. aureus* can grow at a wide range of pH (5–10), the optimal being pH 7.0–7.5 [28]. Acidic conditions could inhibit *S. aureus* growth [29].

A previous study showed that, at first, the infected skin wound is alkaline, and the pH changes to acidic along with bacterial proliferation and then back to alkaline [30]. Therefore, the use of acidic gels can reduce the growth of MRSA to some extent. we hypothesized that HAD hydrogel could inhibit the growth of MRSA biofilm to a certain extent for its acidity. In the colony count tests, the HAD, AMP reduced the MRSA more significantly compared with HAD groups and control groups (Fig. 3f, g and h, $P < 0.05$). Meanwhile, HAD groups reduced the MRSA growth but with no significant difference which indicate acidic gels will inhibit *S. aureus* to a certain degree. RNA-seq based transcriptome analysis was performed on MRSA and HAD, AMP-treated MRSA, and a total of 29,504,404 reads were obtained with a clean ratio of 98.2 %. After mapping the reads, a total of 1647 transcripts were identified in the treated MRSA strain. When compared with the untreated MRSA, 656 genes were differentially expressed, and out of those, 495 (75 %) were down-regulated and 161 (25 %) up-regulated in the selected isolate (Fig. 4a and b). The signal transduction expression heat map is presented in Fig. 4c. As shown in Fig. 4 e and h, the transcripts per million (TPM) of the potassium channel *putP* gene and sodium channel *kdpF* genes reduced significantly in the HAD, AMP-treated group, indicating bacterial communication in MRSA biofilms will be blocked to inhibit the formation of bacterial biofilms. The most common resistance gene is *mecA*. The HAD, AMP-treated group showed no apparent changes compared with untreated MRSA (Fig. 4g), indicating that HAD, AMP exerted no effect on MRSA resistance. These results are consistent with our previous research on bacterial drug resistance experiment. *argA*, *sarR* and *spa* are closely related to bacterial virulence and bacteremia and were down regulated in the HAD, AMP-treated group significantly compared with control groups (Fig. 4f, i and j, $P < 0.05$). In conclusion, HAD, AMP could exert strong anti-biofilm effects by down regulating bacterial communication and MRSA virulence genes.

Journal of Chemical Health Risks

www.jchr.org

JCHR (2024) 14(1), 330-346 | ISSN:2251-6727

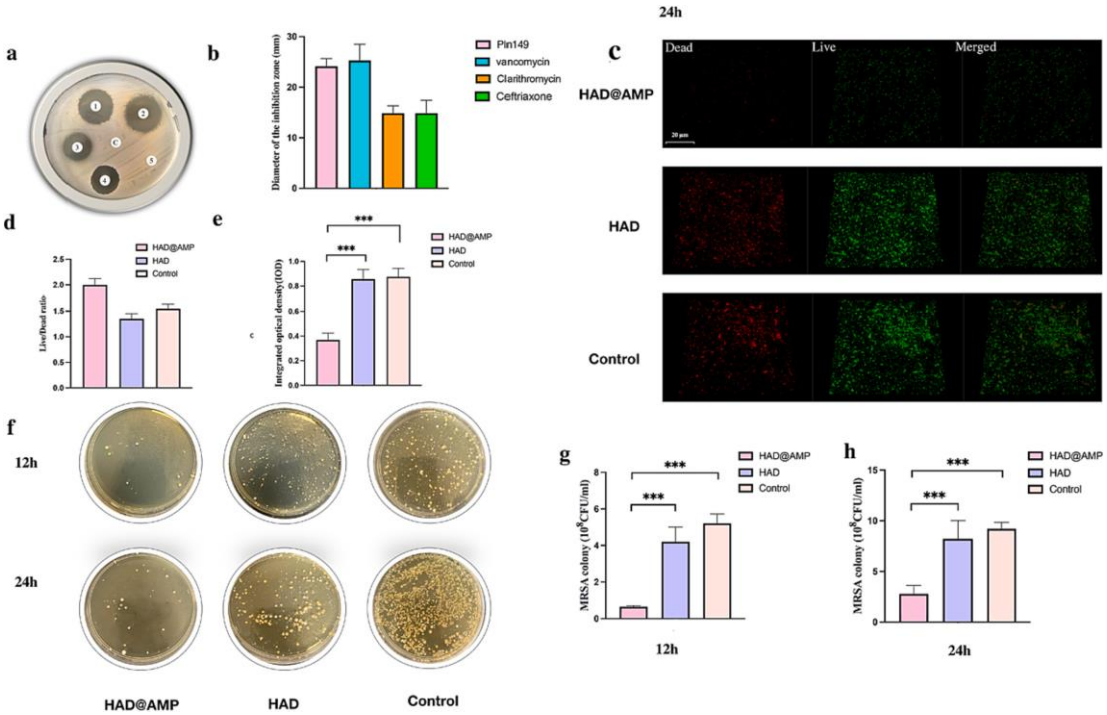

Fig.4. Antibacterial activity and anti-biofilm effects in vitro evaluation. (a) Agar disk diffusion test of Pln149, vancomycin, clarithromycin, and ceftriaxone on MRSA and the associated (b) inhibition zone diameters. (c) Confocal laser microscopy after Live/Dead biofilm staining for 24 h, and (d) the live and dead biofilm ratio comparing MRSA treated with HAD@AMP and untreated. (e) The biofilm integrated optical density (IOD) values. (f) MRSA colonies and (g, h) colony count from different groups for 12 and 24 h. *$P < 0.05$, **$p < 0.01$, and ***$p < 0.001$.

3.3. Wound healing promotion mechanism

RNA-seq based transcriptome analysis was performed on 6 samples of L-929 mouse fibroblasts HAD, AMP-treated. The transcriptome sequencing produced a total of 52.69 Gb of clean data; based on the quantitative expression results, each sample comprised above 6.69 Gb of clean data. The differential gene analysis between HAD, AMP-treated and control groups was performed. As shown in Fig. 5a, there were 1221 differentially-expressed genes (DEGs) statistically significant when comparing HAD, AMP-treated vs. untreated L-929 mouse fibroblasts. Among them, 612 genes were up-regulated and 609 down-regulated (Fig. 5a). After conducting a KEGG enrichment analysis, results showed 231 DEGs enriched in 20 KEGG pathways, including MAPK, PI3K-Akt, AMPK, and ABC transporters pathways (Fig. 5b). Genes involved in inflammation and healing promotion were displayed in a heatmap (Fig. 5c). In the results of GO enrichment, the genes mainly concentrated in the regulation of cell growth, regulation of cell adhesion and positve regulation of cell death (Fig. 5d). TNF-α and IL-6 were the most common pro-inflammatory cytokines in HAD, AMP-treated groups, while TGF-β1 was the most common anti-inflammatory cytokine. Additionally, TNF-α and IL-6 genes were significantly downregulated, and *tgbfb* genes were significantly up-regulated, suggesting that HAD, AMP has marked suppressive effects on inflammation (Fig. 5e, h and j, $P < 0.05$). NF-κB transcription factor regulates multiple aspects of innate and adaptive immune functions and induces the expression of various pro-inflammatory genes. [31] Inflammation could also be regulated in multiple ways indicated by significant downregulation of *nfkib* genes (coding for NF-κB) in the HAD, AMP-treated group (Fig. 5i, $P < 0.05$). Vascular endothelial growth factor-D (VEGFD) is a secreted glycoprotein that activates the endothelium VEGF receptors. and acts as a mitogen, promoting the growth and remodeling of blood and lymphatic vessels. [32]

Journal of Chemical Health Risks

www.jchr.org

JCHR (2024) 14(1), 330-346 | ISSN:2251-6727

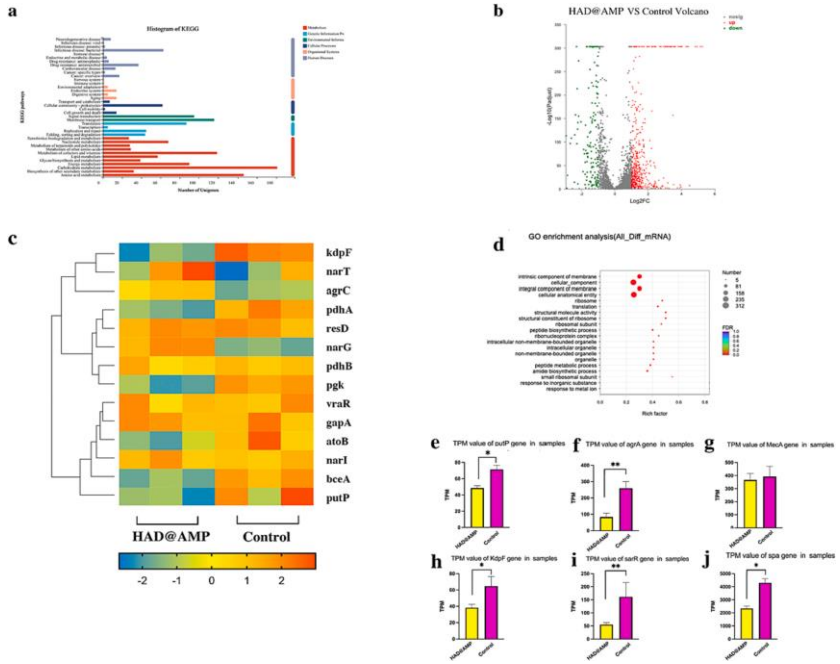

Fig.5. Transcriptome results of MRSA treated by HAD@AMP for 8 h. (a) DEGs KEGG analyses. b) Volcano plot analysis of total DEGs. Untreated MRSA was used as a control. Red and green dots represent down-regulated and up-regulated genes, respectively. Gray dots mark the genes not statistically different. (c) Heatmap of genes associated with signal transduction system. (d) GO enrichment analysis of DEGs. (e-j) MRSA transcripts Per Million (TPM) of (e) *putP*, (f) *agrA*, (g) *mecA*, (h) *kdpF*, (i) *sarR* and (j) *spa*. *P < 0.05, **P < 0.01. (For interpretation of the references to colour in this figure legend, the reader is referred to the web version of this article.)

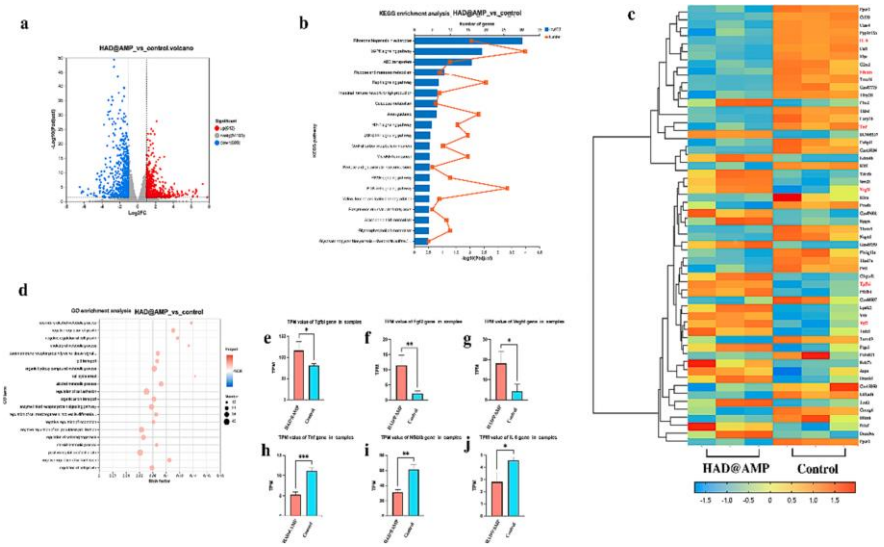

Fig.6. L929 cells transcriptome after HAD, AMP 3-day treatment. (a) Volcano plot analysis of total DEG. Untreated L929 was used as control. Red and green dots represent down-regulated and up-regulated genes, respectively. Gray dots mark the genes not statistically different. (b) DEGs KEGG enrichment analysis of DEGs (c) Heatmap of genes associated with inflammation and defect repair (d) DEGs GO enrichment analysis. (e-j) MRSA Transcripts Per Million (TPM) of (e) *Tgfbi*, (f) *agrA*, (g) *mecA*, (h) *kdpF*, (i) *sarR* and (j) *spa*. *P < 0.05, **P < 0.01, and ***P < 0.001. (For interpretation of the references to colour in this figure legend, the reader is referred to the web version of this article.)

Journal of Chemical Health Risks

www.jchr.org

JCHR (2024) 14(1), 330-346 | ISSN:2251-6727

As a consequence, VEGF-D has been attributed to a broad range of wound-healing properties. A previous study even proposed that VEGF-D could therapeutically enhance the healing of difficult-to-treat cutaneous wounds [33]. In our results, the *vegfd* gene encoding VEGF-D was up-regulated in HAD, AMP - treated L- 929 fibroblasts compared with untreated controls (Fig. 5g, $P < 0.05$). Another major intracellular wound healing effector, the *fgf2* gene, which encodes FGF-2, was also up-regulated (Fig. 5f, $P < 0.05$). In conclusion, the HAD, AMP treatment downregulated the pro-inflammatory genes, up-regulated anti-inflammatory genes, and promoted the expression of genes involved in angiogenesis. L-929 mouse fibroblasts were used to verify HAD, AMP's ability in modulating the overactive inflammatory response in vitro. LPS was used to simulate acidic stress as a result of the local overactive inflammatory response in the intervertebral disc. The Western blot results showed that the expression of inflammatory cytokines IL-6 and TNF-α was significantly reduced in the HAD, AMP group compared with the control group (Fig. 6a, b and c, $P < 0.05$). Moreover, anti-inflammatory TGF-β1 expression was significantly increased compared with the control group (Fig. 6a and d, $P < 0.05$). RT-PCR results were consistent with Western blot results and cell transcriptome sequencing results. RT-PCR findings showed that HAD, AMP specifically inhibits the expression of inflammatory cytokines IL-6 and TNF-α (Fig. 6e and f, $P < 0.05$). On the other hand, HAD, AMP induced the overexpression of anti-inflammatory cytokine TGF-β1 when compared with HAD treatment (Fig. 6g, $P < 0.05$).

3.4. In vivo wound healing evaluation and histology and immunohistochemistry analyses

Skin lesions growth is the most intuitive indicator for wound healing evaluation. In order to evaluate the healing effect in vivo, the wound area was captured and analyzed. Fig. 7 a and b shows wound representative images after MRSA infection and the wound trace during the healing process at days 0, 4, 7, and 10. It is worth noting that the wound areas in both HAD and HAD, AMP groups reduced the affected areas over time, even at various time intervals: HAD group < HAD, AMP group (Fig. 7b). The relevant wound closure ratio in mice under infection is shown in Fig. 7c. After 10 days of treatments, the wound healing rate of HAD, AMP hydrogels was 95.32 ± 2.92 %, considered the best therapeutic effect among the three groups. In addition, as shown in Fig. 4d, the wound areas in the HAD, AMP groups were much smaller than in HAD and control groups at any time point of post-surgery ($P < 0.05$). Meanwhile, the HAD, AMP group showed a remarkable reduction in the wound areas compared to the HAD and control groups (Fig. 7d, $P < 0.05$). We believe this effect is directly related to Pln149 release. Histological analysis was performed to further evaluate the quality of the regenerated tissue in the different groups (Fig. 8a and b). H&E staining was conducted (Fig. 8a), and it was evidenced that, after treatment, the epidermis thickness on day 10 increased significantly in the HAD, AMP groups compared with control and HAD groups (Fig. 8d, $P < 0.05$).

Journal of Chemical Health Risks

www.jchr.org

JCHR (2024) 14(1), 330-346 | ISSN:2251-6727

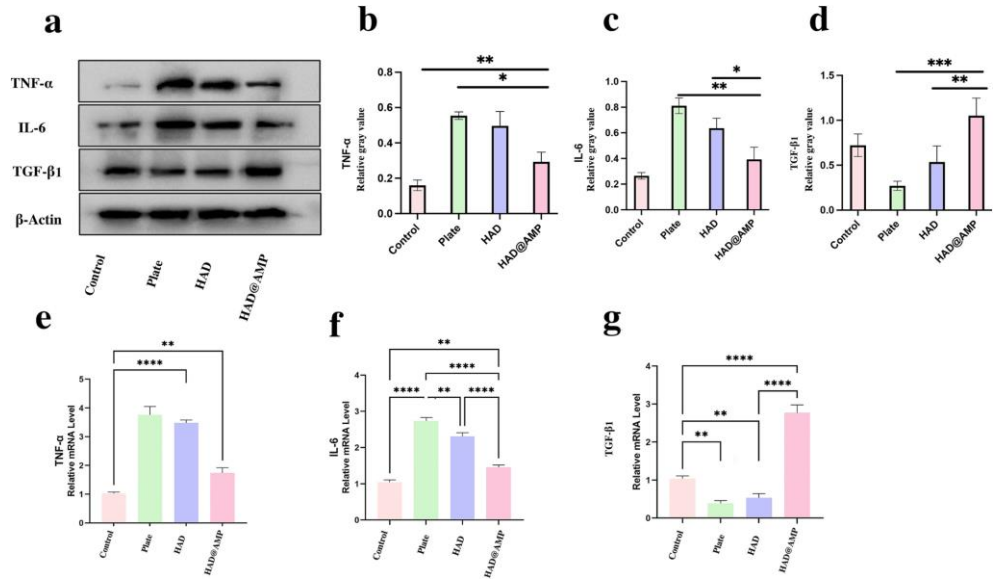

Fig.7. IL-6, TGF-β1, TNF-α expression in L929 cells in LPS inflammatory microenvironment in 7 d. (a) Western blo, the relative level of target protein was normalized to β-actin expression. (b-d) Relative gray value corresponding to Western blot, (e-g) Real-time PCR analysis of the target genes in different samples. *P <0.05, **P < 0.01, ***P < 0.001 and ****P < 0.0001.

In Masson's trichrome staining, a large amount of collagen fibers deposited in the dermal tissue was observed in the HAD, AMP group, while only a few filled the wound sites in the control and HAD groups on day 10 (Fig. 8e, P < 0.05). Although control groups formed the basic epithelium and dermis structure, the dermis was still under repair with a mild inflammatory response. In contrast, the HAD and HAD, AMP groups showed more regular connective tissue and epithelium, with increased fibroblasts presence, new blood vessels, and no obvious inflammatory response, suggesting an excellent wound healing performance, especially when treating with HAD, AMP. TNF-α is an important inflammatory response marker that inhibits wound healing when overexpressed [34]. TGF-β1 is one of the best studied and most widely known anti-inflammatory cytokine, which could exert strong effects in accelerating wound closure, angiogenesis, modulate inflammation [35]. TGF-β1 level is positively correlated with the infectious disease degree. To verify the underlying mechanism of the HAD, AMP hydrogel in preventing infection and reducing inflammation during wound healing in vivo, the mice skin samples were harvested to evaluate IL-10 and TNF-α expression. As shown in Fig. 8c and f, the HAD, AMP treated group showed the lowest TNF-α expression level at day 10 and this was also statistically significant when compared with HAD and control groups (P < 0.05). As presented in Fig. 8g, opposite results for TGF-β1 expression were observed.

The HAD, AMP group showed the highest TGF-β1 level, and the increased expression was significant compared with HAD and control groups (P < 0.05) on the 10th day. These results demonstrated that the HAD, AMP groups was better at suppressing TNF-α, increasing TGF-β1and inhibiting the inflammatory response than the HAD and control groups. The anti-inflammatory effect of HAD, AMP demonstrated the hydrogel's advantages when combined with the AMP sustained release and these results were consistent with Western blot and RT-PCR results which suggested that HAD, AMP effectively inhibited inflammation. CD31 is a platelet-endothelial molecule used as endothelial cells' and angiogenesis marker [36]. As shown in Fig. 5b, staining with CD31 (PECAM) revealed that fibroblasts in the HAD, AMP group's dermis were surrounded with a network of new blood vessels. The CD31 staining showed an increased amount of new blood vessels on day 10 in the wounds treated with the HAD, AMP hydrogel, whereas only a few in the control and HAD groups (Fig. 8c). Elevated CD31 expression in the HAD, AMP-treated group implies

Journal of Chemical Health Risks

www.jchr.org

JCHR (2024) 14(1), 330-346 | ISSN:2251-6727

increased vessel formation with mature structures (Fig. 8h, $P < 0.05$). Above all, the wounds in the HAD, AMP group healed fastest including skin appendage regeneration, by upregulating IL-10 and CD31 expression and down regulating TNF-α expression in vivo.

4. Conclusions

In summary, we have developed an injectable and light curable hyaluronic acid composite gel with an AMP cross-linked with EDC/NHS. HAD, AMP exhibited efficient antimicrobial activity, good histocompatibility, low drug resistance, low bacterial biofilm formation, and enhanced mechanical strength for infected wound healing. During the hydrogel degradation process, the AMP Pln149 is released to inhibit bacterial communication and reduce bacterial biofilm formation. HAD, AMP exhibited excellent antibacterial activity in vitro and in vivo. The typical pro-inflammatory factors (TNF-α, IL-6) were downregulated, while anti-inflammatory factors (TGF-β1) were upregulated. In vivo experiments showed that HAD, AMP significantly stimulated the healing of MRSA-infected wounds compared with control groups, mainly attributed to HAD, AMP's inherent antibacterial and vascularization activity. Additionally, transcriptome results revealed that the hydrogel may promote wound healing by up-regulating VEGF and TGF-β1 signaling and down-regulating NF-κB, TNF-α, and IL-6 signaling. Collectively, the superior biocompatibility and remarkable chronic-wound-healing-promotion effect empower this hydrogel with profound potential for use in wound dressings. This injectable hyaluronic acid composite gel can endow a healthy microenvironment and provide new insight into new skin healing strategies.

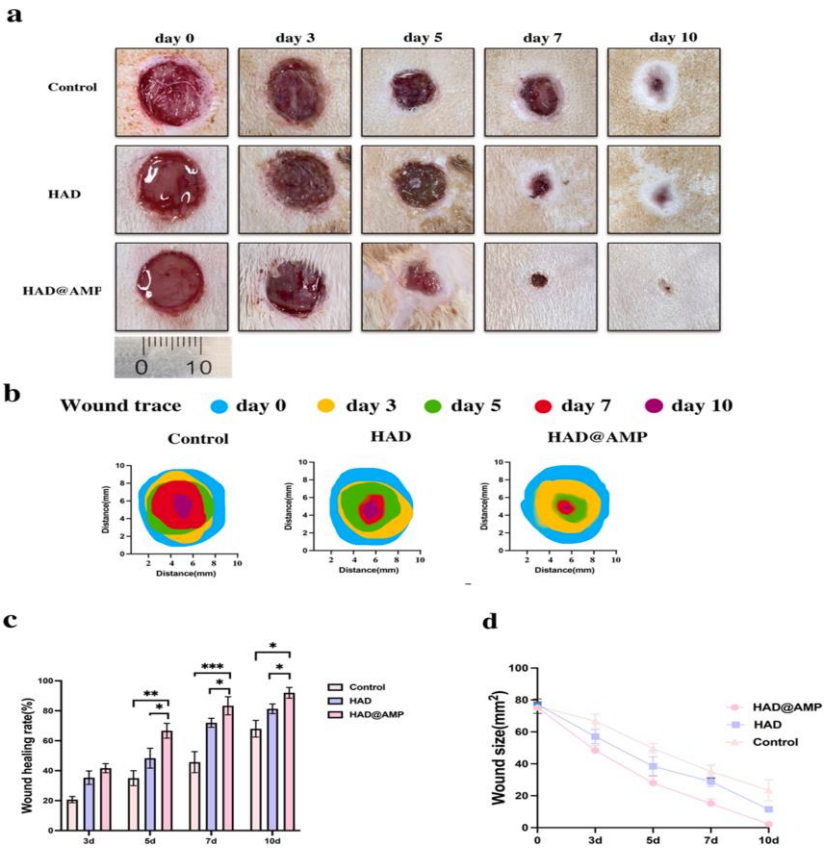

Fig.8. In vivo wound healing studies comparing HAD, HAD, AMP, and control groups. (a) Wound tissues on days 0, 3, 5, 7, and 10, the scale bars are 10 mm. (b) Traces of wound-bed closure during 10 days for three groups. (c) Wound size over time in mice for three groups. (d) Wound healing rate treated with different methods. *$P < 0.05$, **$P < 0.01$, and ***$P < 0.001$.

Journal of Chemical Health Risks

www.jchr.org

JCHR (2024) 14(1), 330-346 | ISSN:2251-6727

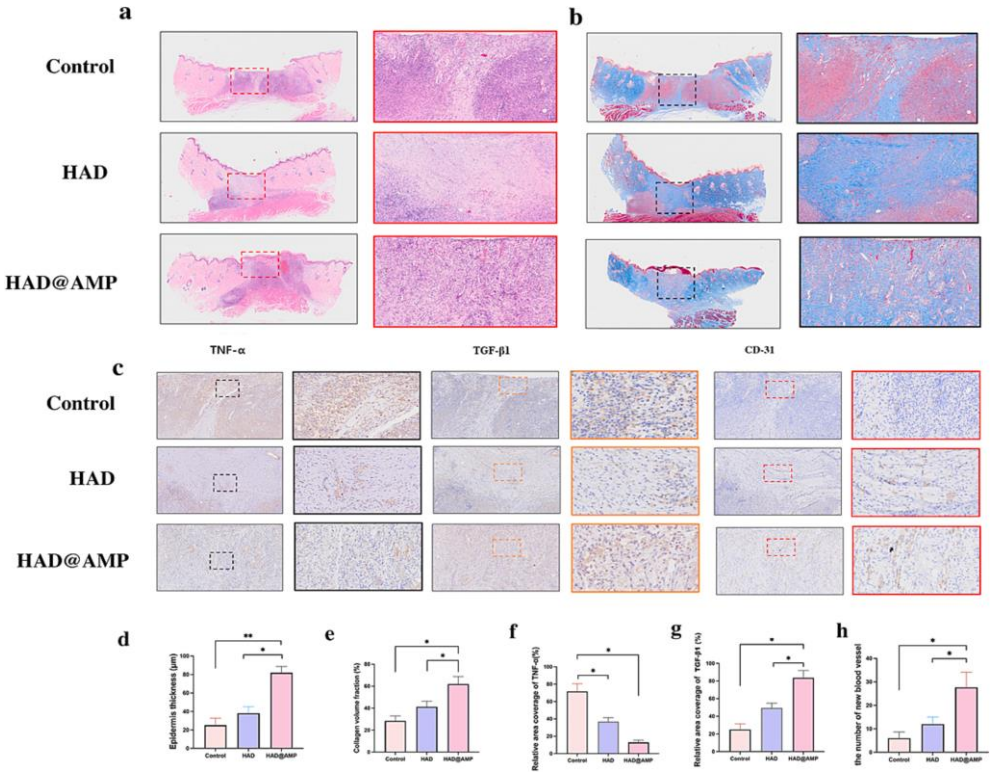

Fig.9. Histological in vivo evaluation of HAD, HAD, AMP, and control groups. (a) Masson staining of wound sites in different groups on day 10. (b) Hematoxylin and eosin (H&E) staining of wound sites in different groups on day 10. (c) Tissue slices stained with TNF-α, TGF-β1 and CD31 immunohistochemistry on day 10. (d) Epidermis thickness of wound sites in different groups on day 10, (e) collagen volume fraction of wound sites in different groups on day 10, and (f-h)TNF-α and IL-10 in the regenerated tissues on day 10. Scale bar = 10 μm, *P < 0.05, **P < 0.01

Declaration of competing interest

The author declares no conflict of interest, financial or otherwise.

Acknowledgements

This research did not receive any specific grant from funding agencies in the public, commercial, or not-for-profit sectors. The authors are helpful to the National Institute of Technology (NIT), Rourkela, Odisha, India for providing all required facilities. The authors would also like to thank to Columbia Institute of Pharmacy, Raipur, Chhattisgarh, India for providing laboratory animal facilities.

References

1. S. Eyerich, et al., Cutaneous barriers and skin immunity: differentiating a connected network, Trends Immunol. 39 (4) (2018) 315–327.
2. T. Eftimov, et al., Long-period gratings and microcavity in-line Mach Zehnder interferometers as highly sensitive optical fiber platforms for bacteria sensing, Sensors 20 (13) (2020) 3772.
3. M. Peetermans, et al., Necrotizing skin and soft-tissue infections in the intensive care unit, Clin. Microbiol. Infect. 26 (1) (2020) 8–17.
4. S. Valderrama-Beltr´ an, et al., Risk factors associated with methicillin-resistant Staphylococcus aureus skin and soft tissue infections in hospitalized patients in Colombia, Int. J. Infect. Dis. 87 (2019) 60–66.
5. S. Mazzariol, et al., Death associated to methicillin resistant Staphylococcus aureus ST8 infection in two dolphins maintained under human care, Italy, Frontiers in Immunology 9 (2018) 2726.
6. N.A. Turner, et al., Methicillin-resistant Staphylococcus aureus: an overview of basic and

Journal of Chemical Health Risks

www.jchr.org

JCHR (2024) 14(1), 330-346 | ISSN:2251-6727

clinical research, Nat. Rev. Microbiol. 17 (4) (2019) 203–218.
7. A.Rochani, et al., Stability-indicating HPLC method to determine the stability of extemporaneously prepared vancomycin oral solution cups, Am. J. Health Syst. Pharm. 79 (1) (2022) e34–e40.
8. M. Erdem Büyükkiraz, Z. Kesmen, Antimicrobial peptides (AMPs): a promising class of antimicrobial compounds, J. Appl. Microbiol. 132 (3) (2022) 1573–1596.
9. J. Lei, et al., The antimicrobial peptides and their potential clinical applications, Am. J. Transl. Res. 11 (7) (2019) 3919.
10. R.K. Thapa, D.B. Diep, H.H. Tønnesen, Topical antimicrobial peptide formulations for wound healing: current developments and future prospects, Acta Biomater. 103 (2020) 52–67.
11. H. Liebl, L.C. Kloth, Skin cell proliferation stimulated by microneedles, Journal of the American College of Clinical Wound Specialists 4 (1) (2012) 2–6.
12. E. Rezvani Ghomi, et al., Wound dressings: current advances and future directions, J. Appl. Polym. Sci. 136 (27) (2019) 47738.
13. S. Pourshahrestani, et al., Polymeric hydrogel systems as emerging biomaterial platforms to enable hemostasis and wound healing, Adv. Healthc. Mater. 9 (20) (2020) 2000905.
14. Y. Liang, et al., Adhesive hemostatic conducting injectable composite hydrogels with sustained drug release and photothermal antibacterial activity to promote full-thickness skin regeneration during wound healing, Small 15 (12) (2019) 1900046.
15. J. Cao, L. Xiao, X. Shi, Injectable drug-loaded polysaccharide hybrid hydrogels for hemostasis, RSC Adv. 9 (63) (2019) 36858–36866.
16. H.F. Darge, et al., Polysaccharide and polypeptide based injectable thermosensitive hydrogels for local biomedical applications, Int. J. Biol. Macromol. 133 (2019) 545–563.
17. A.Sun, et al., Current research progress of photopolymerized hydrogels in tissue engineering, Chin. Chem. Lett. 32 (7) (2021) 2117–2126.
18. X. Lin, et al., Evaluation of the antibacterial effects and mechanism of Plantaricin 149 from lactobacillus plantarum NRIC 149 on the peri-implantitis pathogens, Sci. Rep. 11 (1) (2021) 1–8.
19. A.Sosnik, M.V. Sefton, Semi-synthetic collagen/ poloxamine matrices for tissue engineering, Biomaterials 26 (35) (2005) 7425–7435.
20. M. Soleimani, S. Nadri, A protocol for isolation and culture of mesenchymal stem cells from mouse bone marrow, Nat. Protoc. 4 (1) (2009) 102–106.
21. M. Vambe, et al., Antibacterial screening, synergy studies and phenolic content of seven south African medicinal plants against drug-sensitive and-resistant microbial strains, S. Afr. J. Bot. 114 (2018) 250–259.
22. X. Lin, et al., The effect of five probiotic lactobacilli strains on the growth and biofilm formation of S treptococcus mutans, Oral Dis. 21 (1) (2015) e128–e134.
23. Z. Xia, et al., Transplantation of BMSCs expressing hVEGF165/hBD3 promotes wound healing in rats with combined radiation-wound injury, Int. Wound J. 11 (3) (2014) 293–303.
24. Y. Qiao, et al., Treatment of MRSA-infected osteomyelitis using bacterial capturing, magnetically targeted composites with microwave-assisted bacterial killing, Nat. Commun. 11 (1) (2020) 1–13.
25. M.L. Schweizer, et al., Comparative effectiveness of switching to daptomycin versus remaining on vancomycin among patients with methicillin-resistant *Staphylococcus aureus* (MRSA) bloodstream infections, Clinical Infectious Diseases 72 (Supplement_1) (2021) S68–S73.
26. N.F. Kamaruzzaman, et al., Targeting the bacterial protective armour; challenges and novel strategies in the treatment of microbial biofilm, Materials 11 (9) (2018) 1705.
27. A.Prindle, et al., Ion channels enable electrical communication in bacterial communities, Nature 527 (7576) (2015) 59–63.
28. Valero, et al., Modelling the growth boundaries of Staphylococcus aureus: effect of temperature, pH and water activity, Int. J. Food Microbiol. 133 (1–2) (2009) 186–194.
29. A.I. Hochbaum, et al., Inhibitory effects of D-amino acids on Staphylococcus aureus biofilm development, J. Bacteriol. 193 (20) (2011) 5616–5622.

Journal of Chemical Health Risks

www.jchr.org

JCHR (2024) 14(1), 330-346 | ISSN:2251-6727

30. T. Cui, et al., Micro-gel ensembles for accelerated healing of chronic wound via pH regulation, Adv. Sci. 9 (22) (2022), 2201254.
31. T. Liu, et al., NF-κB signaling in inflammation, Signal Transduct. Target. Ther. 2 (1) (2017) 1–9.
32. M.E. Baldwin, et al., Vascular endothelial growth factor D is dispensable for development of the lymphatic system, Mol. Cell. Biol. 25 (6) (2005) 2441–2449.
33. P.W. Rieck, S. Cholidis, C. Hartmann, Intracellular signaling pathway of FGF-2- modulated corneal endothelial cell migration during wound healing in vitro, Exp. Eye Res. 73 (5) (2001) 639–650.
34. Y. Wang, et al., The role of IL-1β and TNF-α in intervertebral disc degeneration, Biomed. Pharmacother. 131 (2020) 110660.
35. E. Sziksz, et al., Fibrosis related inflammatory mediators: role of the IL-10 cytokine family, Mediators Inflamm. 2015 (2015).
36. G. Musumeci, et al., Enhanced expression of CD31/platelet endothelial cell adhesion molecule 1 (PECAM1) correlates with hypoxia inducible factor-1 alpha (HIF-1α) in human glioblastoma multiforme, Exp. Cell Res. 339 (2) (2015) 407–416